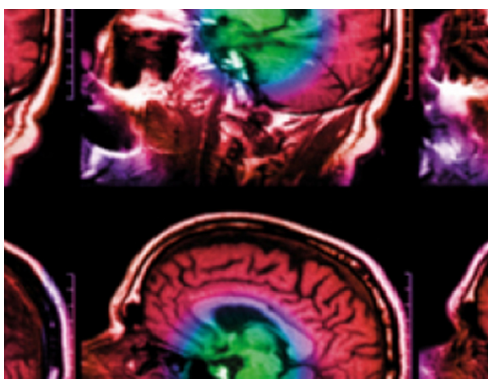


PAPER

# Uncertainty estimation and statistical comparative methodology for mammography x-ray energy spectra

To cite this article: V Santoro-Fernandes *et al* 2020 *Biomed. Phys. Eng. Express* **6** 035018

View the [article online](#) for updates and enhancements.



**IPEM | IOP**

Series in Physics and Engineering in Medicine and Biology

Your publishing choice in medical physics,  
biomedical engineering and related subjects.

Start exploring the collection—download the  
first chapter of every title for free.

# Biomedical Physics & Engineering Express



## PAPER

# Uncertainty estimation and statistical comparative methodology for mammography x-ray energy spectra

RECEIVED  
24 January 2020

REVISED  
23 February 2020

ACCEPTED FOR PUBLICATION  
19 March 2020

PUBLISHED  
22 April 2020

V Santoro-Fernandes<sup>1</sup> , J C Santos<sup>1,2</sup>, L Mariano<sup>1</sup>, V R Vanin<sup>1</sup> and P R Costa<sup>1</sup>

<sup>1</sup> Institute of Physics, University of Sao Paulo, Sao Paulo, Brazil

<sup>2</sup> Institute of Physics, Federal University of Rio de Janeiro, Rio de Janeiro, Brazil

E-mail: [pcosta@if.usp.br](mailto:pcosta@if.usp.br)

**Keywords:** x-ray energy spectra, Monte Carlo simulation, statistical comparison, uncertainty estimation, mammography, x-ray spectrometry, hypothesis testing

## Abstract

Numerical models are an alternative to measurements of x-ray energy spectra when validated by comparative methods that assess the similarity of experimental and calculated spectra. In this work, we compared x-ray energy spectra using several methodologies and determined the methodology with highest statistical power among them. Experiments and Monte Carlo (MC) simulations were used to generate a set of 65 experimental and simulated x-ray mammography spectra pairs typically used in mammography applications. They were generated using Tungsten and Molybdenum targets and Molybdenum and Rhodium filters. The x-ray beams were transmitted through breast tissue equivalent material (bTEM) plates with different glandularities and thicknesses, and the transmitted beam was detected using solid-state x-ray spectrometry with a Cadmium Telluride (CdTe) diode. The MC simulations used the PENELOPE code. Additional uncertainties, beyond that from counting, were propagated using the MC method. Quantitative comparative methods based on the  $\chi^2$  statistics, the first and second half-value layers, the mean energy, the effective energy, and the non-parametric u-test were applied and their specificity (true negative rate) was assessed. The polyenergetic normalized glandular dose (DgNp) to a 6 cm breast of 50/50 glandularity was derived from the spectra. In this work, the  $\chi^2$  statistics attained the highest score; therefore, it is the most indicated metric for the x-ray energy spectra comparative evaluations. The contribution of the additional uncertainties was important, being responsible for up to 98% of the spectra total uncertainty and shifting the mean of the evaluated  $\chi^2$  to 1.2(1), compatible with its expected value. The use of non-parametric test is discouraged by our results, since it failed to distinguish spectra pairs that resulted in up to 72% discrepant DgNp.

## 1. Introduction

The energy spectrum is the most comprehensive characteristic of an x-ray beam. It is also important information for the evaluation of medical image and for dose estimation in several imaging procedures (Hernandez and Boone 2014). The development of numerical models that estimate x-ray energy spectra has been the subject of several works in Medical Physics (Boone and Seibert 1997, Ay *et al* 2004, Delis *et al* 2006, Costa *et al* 2007, Poludniowski 2007, Poludniowski and Evans 2007, Talei and Shariari 2009, Poludniowski *et al* 2009, Bontempi *et al* 2010, Hernandez and Boone 2014, Salvat *et al* 2015,

Hernandez *et al* 2017). Numerical models for x-ray estimation are useful because accurate measurement of x-ray energy spectra is challenging and requires sophisticated spectrometry equipment. Also, the analytical formulation of such spectra is difficult, as noted by Steinbauer *et al* (Steinbauer *et al* 1990), who wrote that a complete analytic treatment of particle scattering seems impossible.

Common numerical methods used to generate x-ray energy spectra are the analytical (or semi-analytical) method (Delis *et al* 2006, Poludniowski *et al* 2009), the empirical (or semi-empirical) model (Boone and Seibert 1997, Costa *et al* 2007, Hernandez and Boone 2014) and Monte Carlo simulation (Booth

*et al* 1986, Agostinelli *et al* 2003, Poludniowski 2007, Poludniowski and Evans 2007, Taleei and Shahriari 2009, Bontempi *et al* 2010, Salvat *et al* 2015, Hernandez *et al* 2017). The spectra generated by these methods can be validated by comparison with experimentally measured spectra (Birch and Marshall 1979, Tomal *et al* 2015). Furthermore, there are cases where spectra generated by different numerical methods are compared with each other (Ng *et al* 2000, Delis *et al* 2006, Poludniowski *et al* 2009, Hernandez and Boone 2014, Hernandez *et al* 2017).

Several methods were used to compare experimental and calculated spectra (Miyajima and Imagawa 2002, Delis *et al* 2006, Morales *et al* 2007, Salehi *et al* 2012). Some researchers compare the plots of two or more spectra based on visual impressions (Miyajima and Imagawa 2002, Morales *et al* 2007, Salehi *et al* 2012, Vidal *et al* 2019), which is practical and intuitive but lacks quantitative information. Others (Birch and Marshall 1979, Poludniowski *et al* 2009, Cunha *et al* 2013, Tomal *et al* 2015, Hernandez *et al* 2017) use spectra derived quantities (SDQs), the most common being: the first and second half-value layers (HVL1 and HVL2), the mean energy (ME) and the effective energy (EE). However, statistical hypothesis tests based on SDQs statistical distributions are rarely conducted, and even their standard deviations are seldomly evaluated (Lépy *et al* 2015). Li *et al* used the relative error statistic (Li *et al* 2017), which provides quantitative information about the comparison, but suffers from the same limitations as the SDQ-based methods. The Mann-Whitney-Wilcoxon non-parametric rank-based statistical test (u-test) (Altman 1991, Bland 2000) was proposed as a comparative methodology for x-ray energy spectra (Delis *et al* 2006, Borrego *et al* 2018). Finally, Ng *et al* (Ng *et al* 2000) pioneered in using the  $\chi^2$  statistic to assess clinical spectra compatibility. It becomes clear that many different comparative methodologies have been employed for the assessment of clinical x-ray spectra similarity, which warrants additional effort to determine which comparative method is ideal for the task. It is reasonable to hypothesize that a channel-by-channel statistical test, such as the  $\chi^2$  test will be more specific than a test using SDQs. Therefore, this work builds on the ground set by Ng *et al* (Ng *et al* 2000), aiming to advance some aspects of this method. However, it was unclear if the variances in the numbers of counts in the spectra could be accurately estimated, which is required to use the  $\chi^2$  test consistently.

In this work we devised an experiment that generated marginally different transmitted experimental spectra; we also used MC simulations to reproduce the experimental setup and to accurately estimate the simulated spectra uncertainties. This allowed us to stress the comparative methodologies and investigate their performance. The polyenergetic normalized glandular dose (DgNp) was derived from the spectra to exemplify a possible clinical impact of failing to choose an accurate spectral comparative methodology. Our

purpose was to determine the best statistical test to compare x-ray mammographic beam energy spectra among the four SDQs mentioned above, the  $\chi^2$  statistic, and the u-test. To our knowledge, this is the first work that compares the performances of the many comparative methodologies that are commonly used.

## 2. X-ray spectra statistical comparative method

In this work, experimental and simulated spectra (examples in figure 3) were compared using several comparative methods. The experimental spectra were measured using a solid-state spectrometer, while the simulated relied on the Monte Carlo (MC) method expanded to account for the uncertainties associated to the input data. The comparative methods used were the nonparametric Mann-Whitney-Wilcoxon u-test; and parametric hypothesis tests using the reduced  $\chi^2$ , HVL1, HVL2, ME and EE statistics. The four later are scalars derived from a spectrum, while the reduced  $\chi^2$  is calculated from a spectra pair as

$$\chi^2 = \frac{1}{N} \sum_{i=1}^N \frac{(C_{e i} - C_{s i})^2}{\sigma_{e i}^2 + \sigma_{s i}^2} \quad (1)$$

where  $N$  is the number of channels in each spectrum, and  $C_{e i}$  and  $C_{s i}$  indicate respectively the counts of the experimental and simulated spectra in channel  $i$ .  $\sigma_{e i}$  and  $\sigma_{s i}$  are the standard deviations associated with  $C_{e i}$  and  $C_{s i}$  respectively.

Although the number of counts in each channel is Poisson distributed, its mean is high in the present case, hence it is well approximated by a normal distribution with variance equal to the observed number of counts, thus the quantity given by (1) is well approximated by a reduced  $\chi^2$  distribution. Moreover, the  $\chi^2$  distribution approaches the normal as the number of degrees of freedom  $N$  increases, being usual to neglect the difference above  $N = 30$  (James 2006); in this work,  $N \geq 239$ . Therefore, we adopt here that  $\chi^2$ , as given by (1), is normally distributed.

Each statistic was compared to its expected value using the z statistic, as it is the standard procedure to compare means of normal distributions with known standard deviation (sd). Because  $N \geq 239$  in this work, the difference between the standard normal distribution and the t-distribution is only marginal. Equations (2) and (3) describe the implementation of the z-test in the cases of the SDQs and reduced  $\chi^2$  statistics.

$$Z_{SDQ} = \frac{SDQ_s - SDQ_e}{\sqrt{\sigma_{SDQ s}^2 + \sigma_{SDQ e}^2}} \quad (2)$$

$$Z_{\chi^2} = \frac{\chi^2 - 1}{\sigma_{\chi^2}}. \quad (3)$$

The reduced  $\chi^2$  statistic is compared to its expected value, 1. The SDQs are compared against each other since they are expected to be the same for the

experimental ( $SDQ_e$ ) and the simulated ( $SDQ_s$ ) spectra. For the Mann-Whitney-Wilcoxon test, the implementation of MATLAB (version R2018b) was used (*ranksum* function). For brevity, we will refer to the reduced  $\chi^2$  simply as  $\chi^2$  henceforth.

The uncertainty in the counts of the experimental spectra ( $\sigma_{e_i}$ ) was evaluated assuming that  $C_{e_i}$  was distributed according to Poisson's statistics. The uncertainty in the counts of the simulated spectra ( $\sigma_{s_i}$ ) was estimated by means of a MC uncertainty propagation technique, which is described in section 3.2.1. Throughout this work, the critical z value used was 3, which yields 99.7% confidence level considering a Normal distribution.

### 3. Experiment and simulation

#### 3.1. Spectroscopic measurements

Mammographic x-ray beams generated using a Mammomat 3000 Nova mammography system (Siemens, Germany, Munich). X-ray beams were generated using an anode composed either of Tungsten or Molybdenum. The used tube has a 1 mm thick Be inherent filtration. Three additional filters were used separately: a 30  $\mu\text{m}$  Mo filter, a 25  $\mu\text{m}$  Rh filter and a 50  $\mu\text{m}$  Rh filter. Three anode-filter combinations were obtained: Mo/Mo, Mo/Rh (25  $\mu\text{m}$ ) and W/Rh (50  $\mu\text{m}$ ). Two tube voltages characteristic of mammographic applications (Pernicka and McLean 2007), 26 and 28 kV, were applied to generate the x-ray beams with current-time products ranging from 100 to 320 mAs.

The x-ray beam was transmitted through breast tissue equivalent material (bTEM) plates. The used bTEM was manufactured by CIRS 012 A<sup>®</sup> (Norfolk, USA) to be equivalent to breast tissue consisting of two glandularities: 30% glandular and 70% adipose tissue (30/70), and 50% glandular and 50% adipose tissue (50/50). The bTEM kit consisted of six slabs: one of thickness equal to 5 mm, two of 10 mm, and three of 20 mm. The surface dimensions of all slabs were 100.0  $\times$  125.5 mm<sup>2</sup>. Spectra of transmitted x-ray beams were measured through bTEM different thicknesses, namely 5, 10, 20, 30, and 40 mm, which were obtained by superimposing bTEM plates. Besides measuring the x-ray energy spectra of beams that were attenuated by bTEM we also measured spectra that were not attenuated by any thickness of bTEM, we henceforth refer to them, respectively, as *transmitted spectra* and *non-attenuated spectra*.

The energy spectra of the transmitted beams were detected using solid-state x-ray spectrometry, as described by Santos *et al* (Santos *et al* 2017). The measuring system was an XR-100 T spectrometer coupled to a PX4 multi-channel analyzer, both manufactured by Amptek Inc. (Bedford, MA). The sensitive element of the spectrometer is a 3  $\times$  3  $\times$  1 mm<sup>3</sup> CdTe crystal, protected by a 1 mm thick Beryllium window. The

frontal aperture of the spectrometer was collimated with centrally bored disks made of a Tungsten, Iron, and Nickel alloy (W 74%, Fe 8% and Ni 18%). The collimation disks' perforation diameters were of 25, 50 and 100  $\mu\text{m}$  and were chosen according to the photon fluence. The collimation prevented high counting rate, reducing pile-up distortions (Bottigli *et al* 2006). Alignment of the spectrometer with the radiation beam was achieved using a method introduced by Santos *et al* (Santos *et al* 2017). The Amptek ADMCA acquisition software was used to register the spectra. A scheme of the experiment is shown in figure 1. The spectrum referring to Mo anode, Mo filtration, 26 kV voltage, 30/70 bTEM glandularity, and 20 mm bTEM thickness could not be included in the analysis because of a data recording error.

The spectrometers embedded pile-up rejection (PUR) feature was kept on. The energy calibration was performed with <sup>241</sup>Am and <sup>152</sup>Eu calibration sources using the transition energies given by (Lépy *et al* 1994, Bé *et al* 2004). In total, 65 spectra were measured in this work.

##### 3.1.1. bTEM composition and composition uncertainty

The bTEM is manufactured using an epoxy resin-based tissue substitute material composed of several low atomic number elements (H, C, N, O, Cl, Ca) homogeneously distributed (White *et al* 1977). The relative atomic composition, mass density, and glandularity of the used bTEM are exhibited in table 1. The weight fraction compositions of the used bTEMs were obtained from Poletti *et al* (Poletti *et al* 2002) and from the datasheet provided by CIRS. We estimated the uncertainty of the elemental compositions from the values provided by these references as

$$\sigma_{Comp.} = \frac{1}{2} |C_m - C_p| \quad (4)$$

where  $C_m$  is the composition provided by CIRS' datasheet and  $C_p$  is from Poletti *et al*.

##### 3.1.2. Correction of detection effects

We used a stripping method, adapted from the procedure described by Di Castro *et al* (Di Castro *et al* 1984), to correct for the spectral detection distortions (Birch and Marshall 1979, Kurková and Judas 2015, Di Castro *et al* 1984, Santos *et al* 2016). The energy-dependent efficiency curves and escape factors used in the corrections were specifically evaluated in the mammographic energy range and for the CdTe detector employed (Tomal *et al* 2012, 2015). We limited the correction to the experimental *non-attenuated x-ray spectra*, which were, after correction, used as *input spectra* for the MC simulations. Neither the simulated nor the experimental transmitted spectra were corrected.

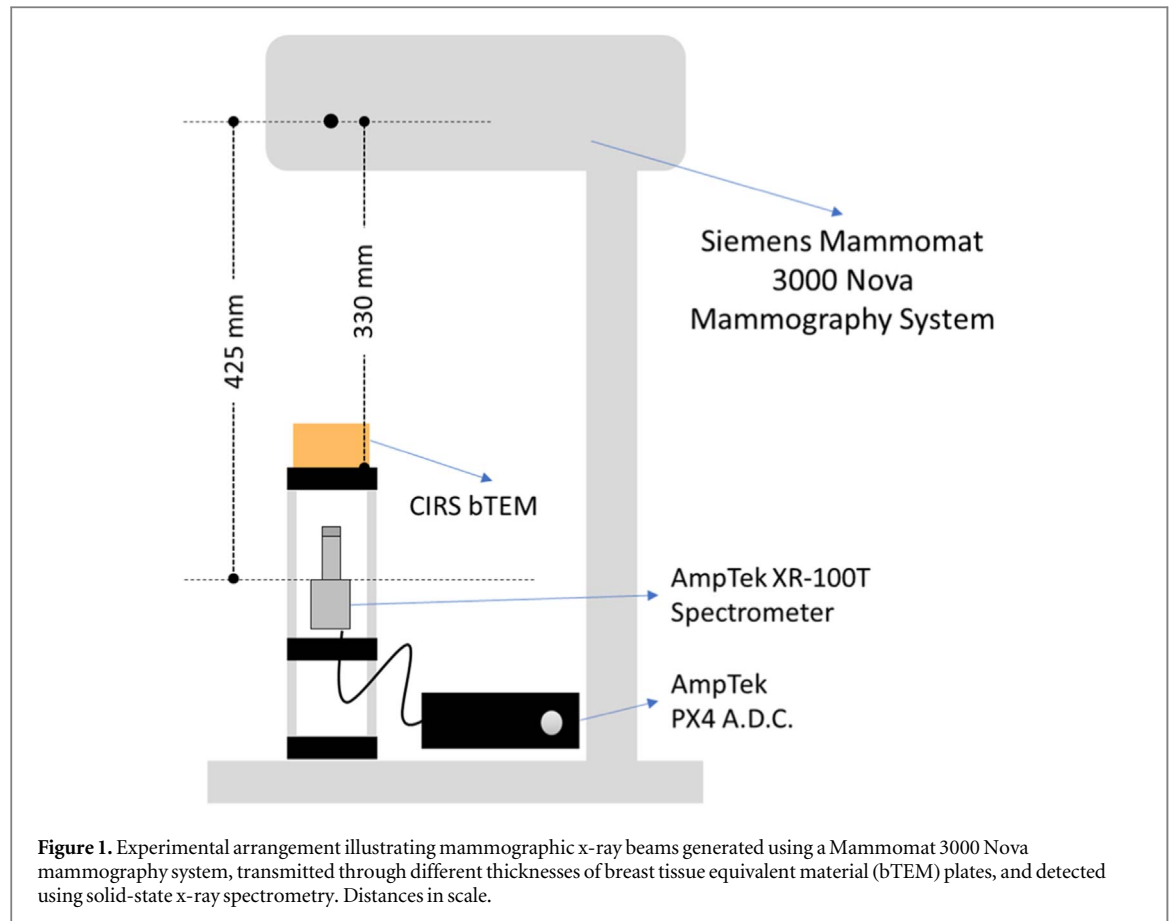


**Table 1.** Weight fraction composition of the bTEM slabs gathered from material's datasheet and published work (Poletti *et al* 2002). Uncertainties are shown in parentheses and correspond to one sd for the work of Poletti *et al*, and to equation (4) for the adopted composition. When not presented, uncertainties were not informed in the original publications. The gray rows show the adopted composition and the relative composition difference between Poletti's and CIRS' datasheet.

Glandularity	Source	H (%)	C (%)	N (%)	O (%)	Cl (%)	Ca (%)	Mass density (g/cm <sup>3</sup> )
30/70	Poletti <i>et al</i> 2002	11.78 (6)	75.12 (7)	0.66 (3)	12.14 (24)	0	0.30 (8)	0.970 (1)
	CIRS' Manual	11.73	75.51	1.23	9.96	1.18	0.35	0.96
	Relative Difference	0.40%	0.50%	46.30%	21.90%	100%	14.30%	1.00%
	Adopted composition	11.73 (2)	75.5 (2)	1.2 (3)	9 (1)	1.2 (6)	0.35 (3)	0.960 (5)
50/50	Poletti <i>et al</i> 2002	11.1 (2)	72.74 (9)	1.04 (4)	14.82 (26)	0	0.30 (8)	0.980 (1)
	CIRS' Manual	11.6	75.07	1.23	10.16	1.17	0.67	0.982
	Relative Difference	4.30%	3.10%	15.40%	45.90%	100%	55.20%	0.20%
	Adopted composition	11.6 (3)	75 (1)	1.23 (9)	10 (2)	1.2 (6)	0.7 (2)	0.982 (1)

### 3.2. Monte Carlo simulation of radiation transport

We used PENELOPE v2011 (Salvat *et al* 2011) MC subroutine package, with the PenEasy v20120601 (Sempau *et al* 2011) steering main program to simulate the detection of energy spectra; the MC simulations' purpose was to reproduce the experimental setup described in section 3.1. The simulations were done using 11 cores of an Intel® Xeon® E5-2420 v2 2.20 GHz CPU, and each MC simulation took 20 h on average to complete. The bTEM composition from the datasheet provided by CIRS was adopted in the simulations. The compositions for the CdTe detector and the Be window of the spectrometer were taken from the material file from PENELOPE's embedded cross-sections database of standard materials, which were

adapted from ESTAR and XCOM (Berger *et al* 2005, 2010).

In our simulations, the energy probability functions of the generated photons were the experimental non-attenuated x-ray spectra after normalization and correction of detection effects. One *input spectrum* was used for each simulated voltage. The virtual x-ray source was positioned in the vertex of a cone, through which the photons propagated, the cone's semi-aperture angle,  $\theta_0$ , was set to 19.98°. This aperture angle yielded in the broad beam configuration, in which the circle formed by the cone's vertical section encompasses the entire bTEM slab surface (figure 2).

A fixed number of  $2 \times 10^{10}$  histories was chosen for each simulation, so that each channel in every

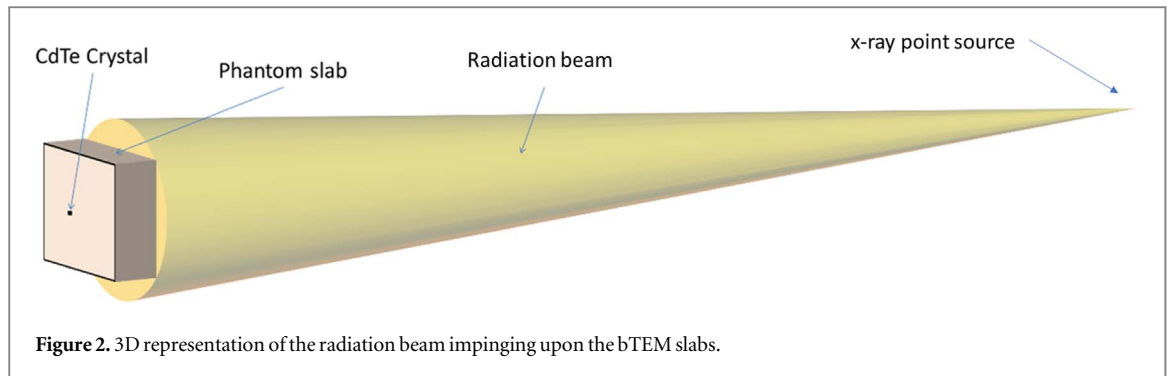


Figure 2. 3D representation of the radiation beam impinging upon the bTEM slabs.

simulated spectrum had more counts than the corresponding channel in the experimental spectrum with which it was compared (homologous spectrum). This assumption assured that the intrinsic Poisson uncertainty of the channels' counts was always lower in the simulated than in the experimental spectrum, for each compared spectra pair. The photon cutoff energy, EABS(ph) simulation parameter, was set to 10 keV at the bTEM and the electron cutoff energy parameter, EABS(e-), was set to 100 keV. PenEasy's PHS script was activated to tally the energy spectra measured in the CdTe crystal. Energy dispersion of 0.06 keV/channel was used, which was the same as in experimental spectra. The collimators used in the frontal aperture of the spectrometer in the experiments were left out of the MC simulations, therefore any detection effect due to transmission and scattering in the collimators was disregarded.

After generation, the MC simulated spectra had its counts normalized to the number of counts in the experimental spectra. Normalization in this context means to minimize the channel by channel squared difference. The minimization was achieved by multiplying all photon counts of the simulated spectra by a constant value  $\hat{\alpha}_0$  obtained by solving the equation

$$\frac{d}{d\alpha_0} \left[ \sum_{i=1}^N (C_{ei} - \alpha_0 C_{si})^2 \right] \Big|_{\hat{\alpha}_0} = 0. \quad (5)$$

This procedure did not change the shape of the simulated spectra, i.e., the count ratio between channels was not altered. The procedure also considers greater weights for the channels with more counts, which hold more information about the spectra.

### 3.2.1. Uncertainty propagation using the MC method

The number of counts in each channel of the energy spectra simulated by an MC code follows a Poisson distribution, therefore its statistical sd is approximately equal to its square root. Nevertheless, other sources can contribute to the uncertainties of the simulated results, as described in the literature (Aguirre *et al* 2016). The uncertainties related to the energy distribution of the initial photons and to the elemental composition of the bTEM were propagated to the MC simulations results. This type A uncertainty

propagation method is similar to that described by Koning and Rochman (Koning and Rochman 2008) and consists of performing several MC simulations varying, within its probability function, the input whose uncertainty is to be propagated. For the photon energies, the varied inputs were the counts per energy channel; they were varied according to a Poisson probability function with parameter equal to the count in each energy channel itself. For the bTEM composition, the varied input was the mass fraction of each element; it was varied according to a normal probability function with mean and sd informed in the 'considered composition' rows of table 1. Each input was individually sampled 25 times.

These MC propagated uncertainties were combined with the Poisson intrinsic uncertainty as follows:

$$\sigma_s^2 = (\sigma_{input}^{\prime 2} - \sigma_{Poisson}^2) + (\sigma_{composition}^{\prime 2} - \sigma_{Poisson}^2) + \sigma_{Poisson}^2 \quad (6)$$

where  $\sigma_s^2$  is the final variance of the simulated spectrum,  $\sigma_{input}^{\prime 2}$  is the variance propagated from the probability function of the initial photon's energy,  $\sigma_{composition}^{\prime 2}$  is the variance propagated from the bTEM composition, and  $\sigma_{Poisson}^2$  is the intrinsic Poisson variance. Considering the correlation between the uncertainty components, the Poisson variance had to be subtracted from the results of MC uncertainty propagation to avoid double counting. Hence, equation (6) simplifies to

$$\sigma_s^2 = \sigma_{input}^2 + \sigma_{composition}^2 + \sigma_{poisson}^2 \quad (7)$$

where the absence of the prime symbol indicates that Poisson variance was already subtracted from the MC estimates.

Instead of a broad photon beam, a narrow beam was used in the MC uncertainty propagation simulations. In the narrow beam configuration, the semi-aperture angle  $\theta_0$  was defined so that its vertical section had a radius of 1.5 mm at the detector surface, which was enough to enclose the entire detector crystal. The cone aperture reduction was implemented because a considerable number of spectra was necessary to estimate the MC uncertainty. Altogether, 25 spectra were simulated for each of the 65 comparisons. As reducing  $\theta_0$  did not alter the mean individual history duration

( $T$ ) the simulation efficiency  $\epsilon$  was improved (Bielajew and Rogers 1988)

$$\epsilon = \frac{1}{T \cdot \sigma^2} \quad (8)$$

where  $\sigma^2$  is the variance of the simulations output, which was reduced by reducing  $\theta_0$ .

### 3.3. Performance of the test: simulation of detection via random sampling

To assess the performance (sensitivity and specificity) of the z-tests and of the u-test, we generated a set of *auxiliary spectra* via simulation of detection and then performed a compatibility test between the experimental spectra set and the auxiliary set. The auxiliary set was simulated based on the experimental set. Sixty-five spectra were simulated by sampling the number of counts in each channel from a Poisson distribution whose mean was the number of counts in each of the homologous experimental channel. We have thus prepared data for a statistical compatibility test that is based on every channel count being a sample of a random variable. The auxiliary spectra were compared to the experimental spectra and all possible experimental-simulated spectra pairs,  $(N^2 + N)/2$  for  $N$  spectra, were tested for compatibility by means of the z-tests and the u-test. The tolerance level for the tests was of 99.7% (critical value = 3 in a standard normal distribution). Each one of the five statistics (HVL1, HVL2, ME, EE and  $\chi^2$ ) was used to perform the comparisons via z-tests. By construction, each spectrum in the auxiliary set is expected to be statistically compatible with its homologous spectrum of the experimental spectra set and to fail the test when compared to any other spectrum. The null hypothesis of the tests was spectra pair compatibility. The alternative hypothesis was spectra incompatibility; hence all tests are two-sided.

The statistical tests used to evaluate the compatibility of a spectra pair either reject or does not reject the null hypothesis, and this decision can be true or false, based on their agreement to the ground truth, which is known for this experiment (only homologous spectra should yield positive comparisons). We then used the power of the test, also named specificity or true negative rate (TNR), to determine the probability of rejecting the null hypothesis when it is wrong (Everitt 2006, p 310, Gueth *et al* 2013, Waghorn *et al* 2011). It is represented as

$$TNR = 1 - \beta = \frac{TN}{TN + FP} \quad (9)$$

where  $\beta$  is the probability of incurring in a type-II error (False Negative - FN).

We also assessed the true positive rate (TPR), also known as sensitivity, which is given by

$$TPR = \frac{TP}{TP + FN} \quad (10)$$

### 3.4. Polyenergetic normalized glandular dose calculation

From the measured non-attenuated energy spectra, we calculated the DgNp,

$$DgNp = \frac{\sum_{E=E_{min}}^{E_{max}} \Phi(E) \vartheta(E) DgN(E)}{\sum_{E=E_{min}}^{E_{max}} \Phi(E) \vartheta(E)}, \quad (11)$$

that would be deposited to 50/50 glandularity breasts of 6 cm thickness (under compression) by using the method proposed by Boone (Boone 2002). In equation (11),  $\Phi(E)$  denotes the photon fluence,  $\vartheta(E)$  is the fluence to exposure converter, and  $DgN(E)$  is the monoenergetic normalized glandular dose. We calculated DgNp based on all the 6 non-attenuated (primary) spectra measured in this work and studied the correlation between DgNp and spectral similarity as indicated by all comparative methods.

## 4. Results and discussion

Some of the measured and simulated spectra, described in sections 3.1 and 3.2 respectively, can be seen in figure 3. The experimental spectrum seen in plot (a) is an example of a non-attenuated spectrum. After being corrected for detection effects, it was used as input for the MC simulations of 26 kV voltage and Mo/Rh anode-filter combination. Thus, the visually observed similarity between the plotted spectra in figure 3(a) indicates that the detection effects were correctly simulated by the MC code system and reintroduced to the detected spectrum in the simulation.

The sd's of the simulated ( $\sigma_{C_s}$ ) and experimental ( $\sigma_{C_e}$ ) spectra counts were combined (the square root of the sum of variances). The combined uncertainties are exhibited in figure 3 as black uncertainty bars associated to the plot of the experimental spectra, with length of one sd. The simulated spectrum is depicted as a solid red line. Plotted below the spectra pairs are their reduced residuals ( $RR$ ), calculated as

$$RR = \frac{C_{si} - C_{ei}}{\sqrt{\sigma_{C_{si}}^2 + \sigma_{C_{ei}}^2}} \quad (12)$$

### 4.1. The uncertainty propagation: investigation of different sources

Uncertainty propagation from the bTEM composition, as mentioned in section 3.1.1, results in an uncertainty in their mass attenuation coefficients  $\left(\frac{\mu}{\rho}\right)$ . These uncertainties are exhibited as uncertainty bars in figure 4.

The relevance of each uncertainty source for the final uncertainty was assessed by calculating the relative uncertainty source contribution. This quantity is shown in figure 5 and is divided into the intrinsic Poisson sd, the sd propagated from the composition of the

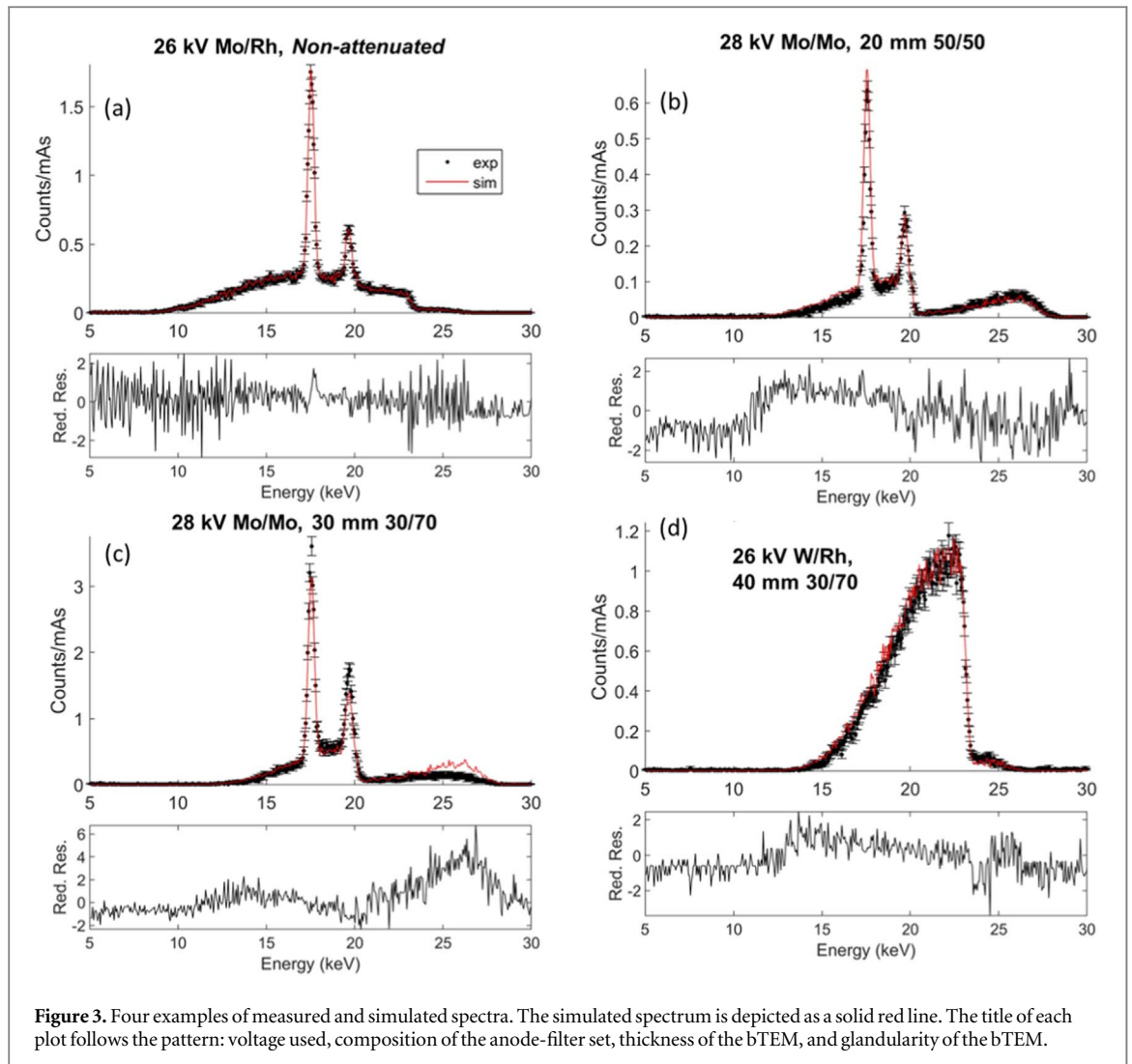


**Figure 3.** Four examples of measured and simulated spectra. The simulated spectrum is depicted as a solid red line. The title of each plot follows the pattern: voltage used, composition of the anode-filter set, thickness of the bTEM, and glandularity of the bTEM.

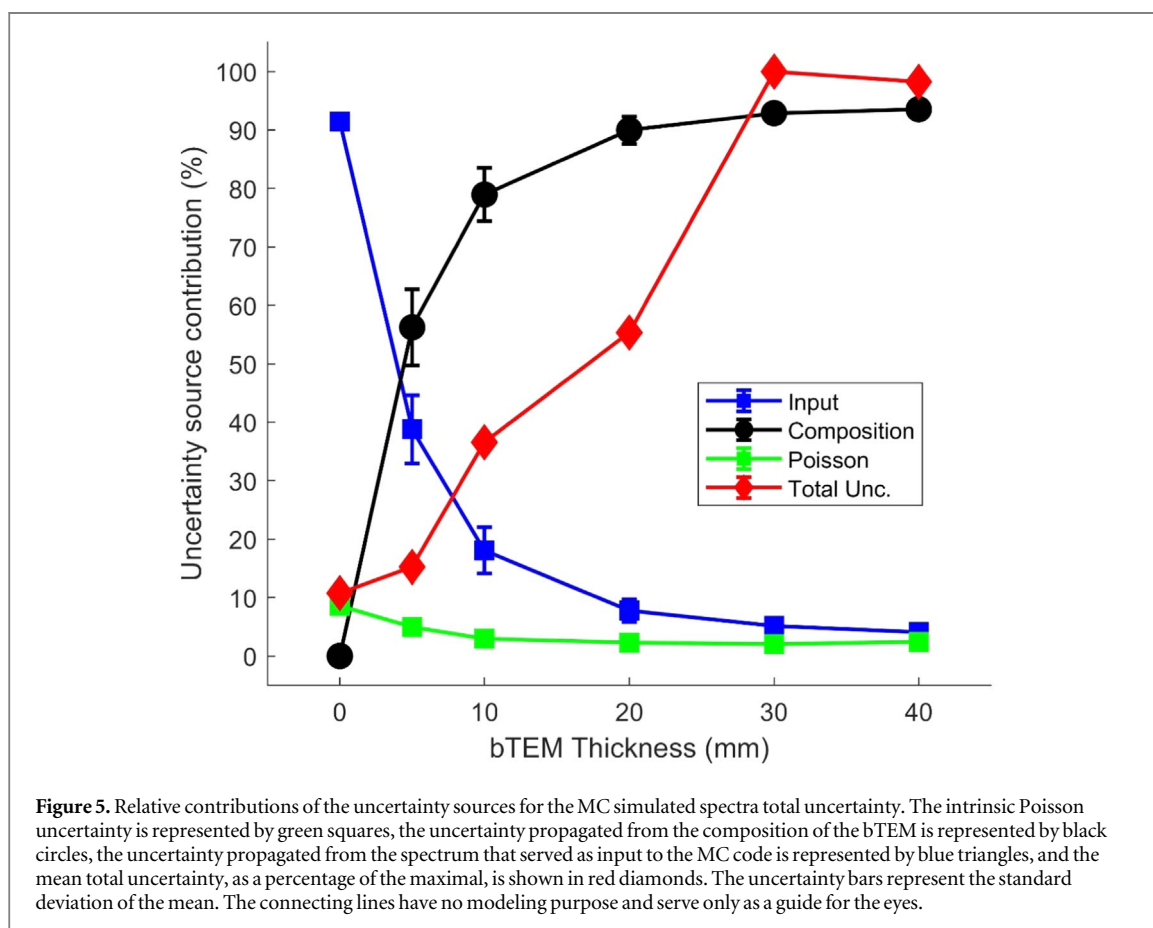
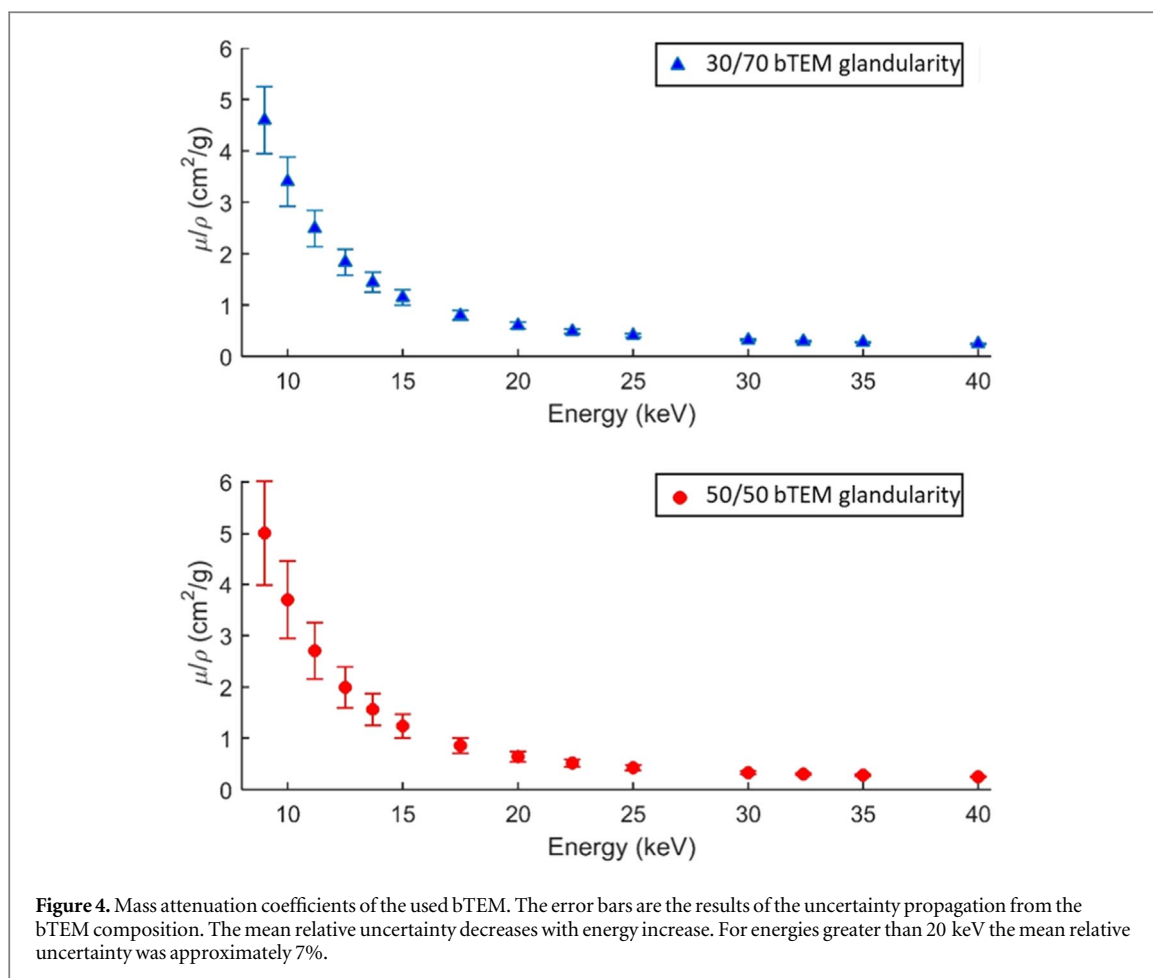
bTEM, and the sd propagated from the input spectrum that served as probability function for the initial photon energy in the simulations. Each point represents a mean calculated with the relative uncertainty contributions of simulations using different anode-filter combinations and bTEM attenuation thicknesses; the uncertainty bar represents the sd of the mean. The intrinsic Poisson sd, which is usually the only one considered, has its higher relative contribution in the case where there is no bTEM attenuation (0 mm thickness). Even in its highest relative contribution, it was responsible for only 10% of the total uncertainty. In the most critical case (20 mm bTEM thickness), neglecting the MC propagated uncertainty would result in a 98% underestimation of the final uncertainty. As expected, as the bTEM thickness increases, the composition uncertainty becomes dominant and the total uncertainty increases considerably.

The input photon energy distributions of the simulations, which were the corrected non-attenuated experimental spectra, and the bTEM compositions were the most relevant of all investigated uncertainty sources. Uncertainties in the cross-sections ( $\approx 1\%$ ) (Aguirre *et al* 2016), in the bTEM dimensions ( $< 0.2\%$ )

and in the bTEM density ( $< 1\%$ ) were also evaluated and found to be relatively small, therefore they were disregarded.

The MC uncertainty propagation method used required a vast number of simulations, hence further development of the MC codes would facilitate the uncertainty estimation task. In future updates, MC codes could be adapted to enable input of the uncertainty of quantities such as material compositions and initial particles energy probability function.

Additional uncertainty estimation for the MC spectra caused the distribution of the 65  $\chi^2$  values, obtained as described in section 2, to shift towards the theoretical predicted distribution (the  $\chi^2$  statistic is expected to follow a probability density function with mean equal to 1). This can be seen in figure 6, where two different histograms are superimposed: one considering Poisson uncertainty alone, and another where Poisson uncertainty was combined with the MC propagated uncertainties. The change in the behavior of the mean of the distribution with and without the use of the MC propagated uncertainty is evident: the mean decreased from 3.2(2), which is not compatible to the  $\chi^2$  expected value, to 1.2(1), which is compatible to the



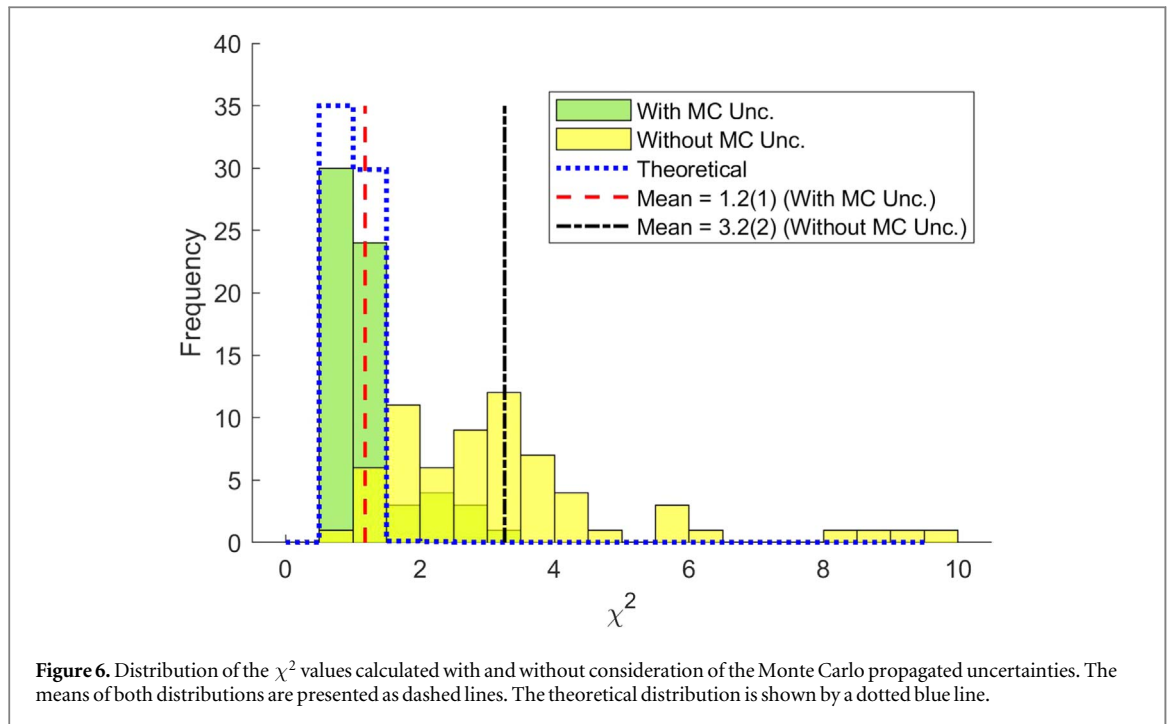


**Figure 6.** Distribution of the  $\chi^2$  values calculated with and without consideration of the Monte Carlo propagated uncertainties. The means of both distributions are presented as dashed lines. The theoretical distribution is shown by a dotted blue line.

**Table 2.** True negative (TN), false positive (FP), true negative rate (TNR), and true positive rate (TPR) results from the u-test and the z-tests done using five statistics, namely the  $\chi^2$ , the first and second half-value layers, the mean energy and the effective energy. The tolerance level used was 99.7%. Note that the maximal rate of true negatives is 0.97 since the diagonal values must be positive.

	$\chi^2$	HVL1	HVL2	ME	EE	U
TN	0.97	0.93	0.90	0.93	0.93	0.42
FP	0	0.04	0.07	0.04	0.04	0.52
TNR	1	0.96	0.93	0.96	0.96	0.44
TPR	1	1	1	1	1	1

expected value; the uncertainties in parenthesis correspond to one sd. An accurate method of uncertainty estimation, rather than using only Poisson's uncertainty, improved the reliability of the test when comparing energy spectra.

The  $\chi^2$  values obtained in this work are in disagreement with the ones from Ng. *et al* work (Ng *et al* 2000). There, all  $\chi^2$  values were equal to one when rounded to integers. A broader distribution of  $\chi^2$  values was observed here (figure 6). Ng *et al* considered that only Poisson uncertainty was associated to the simulated spectra. However, we took into account the uncertainties in the x-ray photon source energy spectrum and bTEM composition, which revealed to be more important than the Poisson photon counting uncertainty.

#### 4.2. Performance of the test: dependence with test statistic

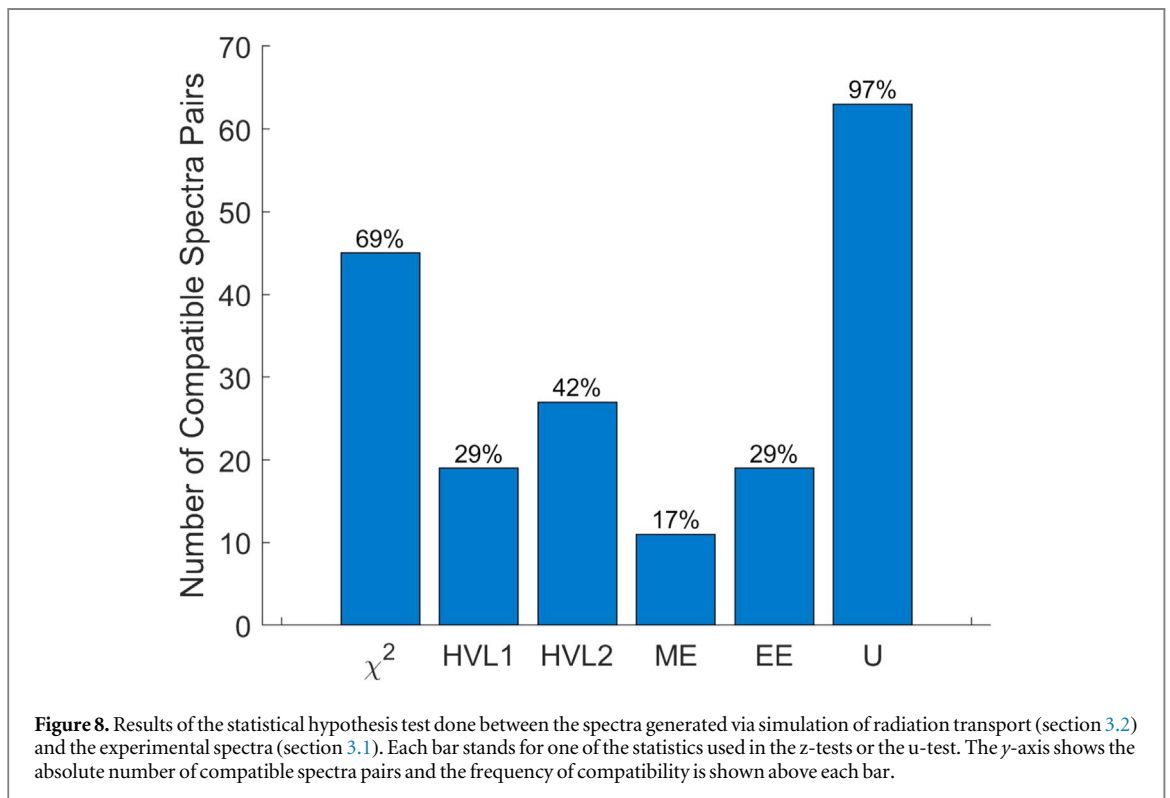
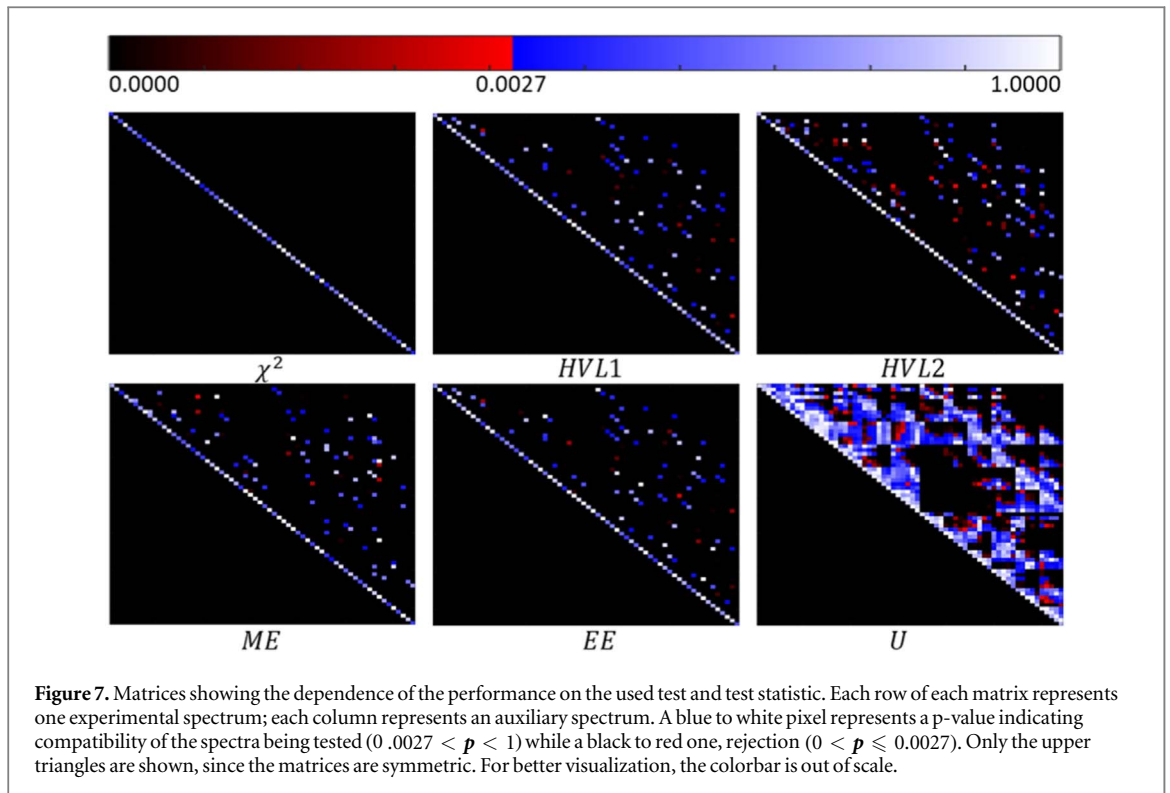
Regarding the performance of the tests described in section 3.3, the  $\chi^2$  was the statistic with the highest TNR score and resulted in the maximal score in the TNR ( $TNR = 1$ ), as presented in table 2. Altogether,

2145 statistical comparisons were made for each of the 5 statistics. These results can be represented in symmetric p-value matrices, as the ones seen in figure 7, where each row represents one experimental spectrum and each column represents an auxiliary spectrum. Different color schemes were chosen to represent compatibility (blue to white) and rejection (black to red) when performing the hypothesis test; as stated in section 2, the critical z value used was 3, which yields 99.7% confidence level considering a normal distribution. Since the matrices are symmetric, we set all values of the lower triangle to zero. By construction, it is expected that the diagonals of the matrices are composed by elements indicating compatibility and that the off-diagonal elements indicate rejection. Discordance from the expectations imply in FPs or FNs.

The matrices make it evident that all statistics, other than the  $\chi^2$ , showed flawed performance in testing these spectra set for compatibility, reducing the test's TNR. However, none of the statistics used in the test resulted in FN. Therefore, all statistics yielded the maximal TPR, as seen in table 2 and is observable from the diagonals of the matrices in figure 7. The non-parametric test matrix (indicated by an U) showed the greatest number of spurious compatibilities, showing that, this nonparametric test is less specific than the parametric tests, as also observed from table 2.

#### 4.3. Comparison of MC simulations to measured spectra

When comparing the spectra generated via simulation of radiation transport (section 3.2) to the experimental set (section 3.1), we have seen that the parametric statistical hypothesis tests based on the  $\chi^2$  statistics



showed the highest number of compatibility results among the tested spectra, as is illustrated in figure 8. The  $\chi^2$  statistic provides a more specific test, therefore, all other statistics used in the parametric test underestimate the ability of the used MC method to simulate the x-ray beam of the mammography equipment. On the other hand, the nonparametric u-test rejected fewer spectra

(97% compatibility); however, we learned from the results in section 4.2 that this test is overly conservative, with relatively low TNR when compared to the parametric tests. Therefore, the high compatibility indicated by the u-test is to be expected and spectra comparisons using this test are much less informative than the other methods presented in this work.

**Table 3.** Table with the results of comparisons between measured and MC simulated spectra using the z-test with the  $\chi^2$  statistic. A green C stands for compatible spectra pair, a red R + stands for a rejected comparison where  $\chi^2 > 1$ , a blue R- stands for a rejected comparison where  $\chi^2 < 1$ , and a gray cell is a missing datum.

voltage	Anode-filter	Non-Attenuated	50/50 glandularity					30/70 glandularity				
			5 mm	10 mm	20 mm	30 mm	40 mm	5 mm	10 mm	20 mm	30 mm	40 mm
26 kV	Mo/Mo	R-	C	C	C	C	C	C	C		C	C
	Mo/Rh	R-	C	C	C	R-	R-	C	C	C	C	C
	W/Rh	R-	C	C	C	C	R-	C	C	C	C	C
28 kV	Mo/Mo	C	C	C	C	C	C	R+	R+	C	R+	R+
	Mo/Rh	R-	C	C	C	C	C	R+	R+	C	R+	R+
	W/Rh	R-	C	C	R-	C	C	C	C	R+	R+	R+

The obtained results suggest that the  $\chi^2$  is the most indicated statistic to perform a quantitative and accurate statistical compatibility test, among the test statistics. The  $\chi^2$  does a channel by channel comparison of the energy spectra, leading to the higher power of the hypothesis test, under the null hypothesis. As shown in table 2, the use of the  $\chi^2$  statistic avoids ambiguities such as morphologically different energy spectra that yield SDQ similar enough to pass a compatibility test, given their uncertainties.

Even though this work tested the  $\chi^2$  method only in the mammographic energy range and with mammographic parameters, we see no statistical or physical reason to believe that the comparative method used in this work could not be applied to clinical x-ray imaging procedures other than mammography. The used statistical framework is not specific to mammography spectra, and the physics of x-ray generation, i.e. Bremsstrahlung and characteristic x-ray emission, is similar in various x-ray applications, e.g. CT and projection radiography. In MC simulations of x-ray beams, it is common to estimate the input probability distribution of the MC photons energy via simulation of the Bremsstrahlung in the anode of the x-ray source (Ng *et al* 2000, David *et al* 2012). Such simulations are time-consuming and usually adopt interaction-forcing mechanisms to increase the Bremsstrahlung yield and speed up the simulation, introducing inaccuracies in the MC results. Our method avoids these inaccuracies but must deal with experimental detection effects, which were corrected by the stripping procedure mentioned in section 3.1.2.

In assessing compatibility via a hypothesis test, a tolerance level of 99.7% was adopted. The employment of this type of test is new for clinical spectra comparison, we did not find literature-based evidence about the most appropriate choice for the critical value. Borrego *et al* used a 95% tolerance interval, which is stricter than the one we used; however, they don't discuss the rationale for this choice and the non-parametric test used by them was shown to be rather

conservative. It is beyond the scope of this work to determine which tolerance level should be used for each of the many possible applications for the x-ray energy spectra. Furthermore, as in all statistical hypothesis test, the tolerance level must be tailored for each particular application.

The spectra simulated via MC were compared to the measured spectra using the methodology described in section 3.1. Results for comparisons using the  $\chi^2$  statistic are shown in table 3.

Some trends on rejection were apparent. For example, the bTEM with 30/70 glandularity had 11 out of 20 rejections; all of these 11 rejections were in the 28 kV voltage and they were all caused by a  $\chi^2 > 1$ . All the 4 rejections that happened when using bTEM of 50/50 glandularity were caused by  $\chi^2 < 1$ . Furthermore, the 28 kV voltage had 14 out of the 20 rejections. Moreover, 5 out of the 6 *non-attenuated* spectra were rejected; visual inspection of these spectra shows an apparent concordance between the curves, one example of *non-attenuated* spectra is shown in figure 3(a). Also, all five spectra were rejected for having too small of a  $\chi^2$  ( $\approx 0.7$ ), suggesting that the uncertainty for these spectra is overestimated. Not accounting for covariances in the uncertainty propagation is a likely cause for the overestimation of the uncertainties of the *non-attenuated* spectra and of the spectra using bTEM of 50/50 glandularity. Based on the results shown in table 3, we infer it is likely that PENELOPE is more accurate in simulating the x-ray spectra transmitted through 50/50 glandularity phantoms than those transmitted through 30/70 glandularity phantoms; however, studying the reasons for this performance discrepancy is beyond the scope of this work.

Visual examination of the spectra with the greatest incompatibility, shown in figure 3 (c), suggests that visual intuition is well represented by the z-test using  $\chi^2$  statistic, because incompatibilities in the spectral shape are easily observed. However, the z-test brings an additional advantage of allowing for quantification

**Table 4.** P-values of comparison of non-attenuated spectra pairs using the non-parametric u-test, the parametric z-test with  $\chi^2$ , HVL1, HVL2, ME, and EE; and the p-value for testing DgNp derived from each spectra pair. Values indicated by a zero are smaller than  $1 \times 10^{-300}$ . Red numbers indicate p-values greater than 0.0027.

Spectra pair (anode-filter and voltage)		DgNp	U	$\chi^2$	HVL1	HVL2	ME	EE
Mo/Mo 26 kV	Mo/Mo 28 kV	3.9E-02	1.5E-01	0	0	0	0	0
Mo/Mo 26 kV	Mo/Rh 26 kV	6.6E-03	2.4E-01	0	0	0	0	0
Mo/Mo 26 kV	Mo/Rh 28 kV	2.6E-05	8.8E-02	0	0	0	0	0
Mo/Mo 26 kV	W/Rh 26 kV	6.4E-13	1.3E-01	0	0	0	0	0
Mo/Mo 26 kV	W/Rh 28 kV	0	3.0E-01	0	0	0	0	0
Mo/Mo 28 kV	Mo/Rh 26 kV	5.1E-01	6.4E-03	0	3.2E-03	1.8E-01	6.7E-08	1.1E-03
Mo/Mo 28 kV	Mo/Rh 28 kV	2.8E-02	6.1E-01	0	0	0	0	0
Mo/Mo 28 kV	W/Rh 26 kV	1.2E-07	6.5E-01	0	0	0	0	0
Mo/Mo 28 kV	W/Rh 28 kV	3.8E-13	1.4E-03	0	0	0	0	0
Mo/Rh 26 kV	Mo/Rh 28 kV	1.2E-01	3.2E-01	0	0	0	0	0
Mo/Rh 26 kV	W/Rh 26 kV	2.9E-06	4.5E-03	0	0	0	0	0
Mo/Rh 26 kV	W/Rh 28 kV	5.5E-11	1.7E-03	0	0	0	0	0
Mo/Rh 28 kV	W/Rh 26 kV	1.7E-03	9.6E-01	0	0	3.9E-08	8.3E-14	0
Mo/Rh 28 kV	W/Rh 28 kV	1.7E-06	1.0E + 00	0	0	0	0	0
W/Rh 26 kV	W/Rh 28 kV	2.1E-01	5.2E-01	0	0	0	0	0

of the similarity, so that the experimenter can distinguish between simulation models in their ability to simulate the measured data.

#### 4.4. Example of clinical impact: polyenergetic normalized glandular dose

The cross-comparison of the 6 non-attenuated experimental spectra and their DgNps resulted in 15 comparison pairs. The p-values for intercomparing the spectra using all six comparative methods studied in this work, and the p-value for testing the DgNp using a z-test, are shown in table 4.

Nine out of the 15 comparisons resulted in significantly different DgNps. The u-test wrongfully indicated compatibility (false positive decision) of 13 spectra pairs out of the 15 cross-comparisons. Seven of these 13 false positives had significantly different DgNp. The most extreme case happened between the spectrum generated with Mo/Mo anode-filter and 26 kV voltage and the spectrum generated with W/Rh and 28 kV, for which the DgNps were respectively 0.136(6) and 0.233(8) mGy/mGy, the dose deposited by the latter was 72% greater. All other comparative methodologies succeeded in distinguishing spectra pairs that resulted in significantly different DgNps; however, our results (section 4.2) show that the  $\chi^2$  is the most indicated choice for spectra comparison. The other comparative methodologies can be flawed, proof of this is the HVL1 and HVL2 tests failing in distinguishing the Mo/Mo 28 kV and the Mo/Rh 26 kV non-attenuated spectra. Although in this particular instance they resulted in undistinguishable DgNps, spectra with same HVL can result in different DgNps delivered to materials other than aluminum. In summary, despite being challenging because of the necessity of accurate uncertainty estimation, the  $\chi^2$  comparative methodology should be chosen, especially when the

application requires subtle spectral differences to be detected.

## 5. Conclusion

Our results suggest that a parametric hypothesis test that uses the  $\chi^2$  statistics is the most indicated to compare clinical x-ray energy spectra, when the uncertainties in the arrangement are propagated to the compared quantities. The method has been tested in a set of spectra pairs and yielded, with the  $\chi^2$  variable, the highest result amongst all other variables: HVL1, HVL2, ME and EE. The non-parametric u-test showed the worst overall results, we have shown that it is unable to distinguish between spectra that result in extremely different dose depositions. Even though all parametric tests achieved a high TNR ( $> 0.9$ ), using the  $\chi^2$  variable lead to the highest possible score ( $TNR = 1$ ). The accurate uncertainty estimation is a crucial step to adopt the  $\chi^2$  distribution for spectra comparison, and it was responsible for shifting the  $\chi^2$  distribution mean to 1.2(1), compatible with the expected value. We found that the variance in experimental spectra Poisson counting statistics alone is an order of magnitude smaller than the total variance in the differences between simulated and experimental x-ray energy spectra and the total variance increases with bTEM thickness. We suggest that future releases of Monte Carlo radiation transport implementations could allow for input of the uncertainties associated to the simulation parameters.

## Acknowledgments

The authors would like to acknowledge the Nuclear Technology Development Center; FAPESP funding agency for the partial funding under projects number

2013/07117-0 and research regular project 2010/12237-7; CAPES funding agency for the grants received during the realization of this project, CNPQ for research grants 167332/2014-7 and 315096/2018-7, and CNPQ/FAPESP funding of the project by INCT - Metrology of Ionizing Radiation in Medicine (grant number 2008/57863-2). We would like to thank Dr José M Fernández-Varea for his scientific support regarding the use of PENELOPE, for his kind review of the manuscript, and for his hospitality during V Santoro-Fernandes stay in the University of Barcelona.

## ORCID iDs

V Santoro-Fernandes  <https://orcid.org/0000-0001-6965-0448>

V R Vanin  <https://orcid.org/0000-0002-6666-4155>

## References

- Agostinelli S et al 2003 GEANT4 - a simulation toolkit *Nucl. Instruments Methods Phys. Res. Sect. A Accel. Spectrometers, Detect. Assoc. Equip.* **506** 250–303
- Aguirre E, David M, DeAlmeida C E and Bernal M A 2016 Impact of photon cross section uncertainties on Monte Carlo-determined depth-dose distributions *Phys. Medica* **32** 1065–71
- Altman D G 1991 *Practical Statistics for Medical Research* (London: Chapman and Hall)
- Ay M R, Shahriari M, Sarkar S, Adib M and Zaidi H 2004 Monte Carlo simulation of x-ray spectra in diagnostic radiology and mammography using MCNP4C *Phys. Med. Biol.* **49** 4897–917
- Bé M M, Chisté V, Dulieu C, Browne E, Chechev V, Kuzmenko N, Helmer R, Nichols A, Schönfeld E and Dersch R 2004 Table of radionuclides (Vol 2-A = 151 to 242) *Bur. Int. des poids Mes.* 21–282
- Berger M J, Coursey J S, Zucker M A and Chang J 2005 ESTAR, PSTAR, and ASTAR: computer programs for calculation stopping-power and range tables for electrons, protons, and helium ions *Natl. Inst. Stand. Technol.* <http://physics.nist.gov/Star>
- Berger M J, Hubbell J H, Seltzer S M, Chang J, Coursey J S, Sukumar R, Zucker D S and Olsen K 2010 XCOM: photon cross sections database *NIST Stand. Ref. Database* **8** <http://nist.gov/pml/data/xcom/index.cfm>
- Bielajew A F and Rogers D W O 1988 *Variance Reduction Techniques Monte Carlo Transport of Electrons and Photons* (US: Springer) pp 407–19
- Birch R and Marshall M 1979 Computation of bremsstrahlung x-ray spectra and comparison with spectra measured with a Ge(Li) detector *Phys. Med. Biol.* **24** 505–17
- Bland M 2000 *Introduction to Medical Statistics* 46 (London: Oxford University Press)
- Bontempi M, Andreani L, Rossi P L and Visani A 2010 Monte Carlo simulator of realistic x-ray beam for diagnostic applications *Med. Phys.* **37** 4201–9
- Boone J M 2002 Normalized glandular dose (DgN) coefficients for arbitrary x-ray spectra in mammography: computer-fit values of Monte Carlo derived data *Med. Phys.* **29** 869–75
- Boone J M and Seibert J A 1997 An accurate method for computer-generating tungsten anode x-ray spectra from 30 to 140 kV *Med. Phys.* **24** 1661–70
- Booth T E et al 1986 *MCNP-A General Monte Carlo Code for Neutron and Photon Transport* ed J F Briesmeister (Los Alamos National Laboratory)
- Borrego D, Lowe E M, Kitahara C M and Lee C 2018 Assessment of PCXMC for patients with different body size in chest and abdominal x-ray examinations: a Monte Carlo simulation study *Phys. Med. Biol.* **63** 065015
- Bottigli U, Golosio B, Masala G L, Oliva P, Stumbo S, Delogu P, Fantacci M E, Abbene L, Fauci F and Raso G 2006 Comparison of two portable solid state detectors with an improved collimation and alignment device for mammographic x-ray spectroscopy *Med. Phys.* **33** 3469–77
- Costa P R, Nersissian D Y, Salvador F C, Rio P B and Caldas L V E 2007 Generation of calibrated tungsten target x-ray spectra: modified TBC model *Health Phys.* **92** 24–32
- Cunha D M, Tomal A and Poletti M E 2013 Monte carlo simulation of x-ray spectra in mammography and contrast-enhanced digital mammography using the code PENELOPE *IEEE Trans. Nucl. Sci.* **60** 495–502
- Di Castro E, Pani R, Pellegrini R and Bacci C 1984 The use of cadmium telluride detectors for the qualitative analysis of diagnostic x-ray spectra *Phys. Med. Biol.* **29** 1117–31
- David M G, Pires E J, Albuquerque M A, Magalhães L A, Bernal M A, Peixoto J G and De A C E 2012 Spectra and depth-dose deposition in a polimethylmetacrilate breast phantom obtained by experimental and Monte Carlo method *Rev. Bras. Física Médica* **6** 29–33
- Delis H, Spyrou G, Costaridou L, Tzanakos G and Panayiotakis G 2006 Suitability of new anode materials in mammography: dose and subject contrast considerations using Monte Carlo simulation *Med. Phys.* **33** 4221–35
- Everitt B S 2006 *The Cambridge Dictionary of Statistics* 94 (New York: Cambridge University Press)
- Gueth P, Dauvergne D, Freud N, Letang J M, Ray C, Testa E and Sarrut D 2013 Machine learning-based patient specific prompt-gamma dose monitoring in proton therapy *Phys. Med. Biol.* **58** 4563–77
- Hernandez A M and Boone J M 2014 Tungsten anode spectral model using interpolating cubic splines: unfiltered x-ray spectra from 20 kV to 640 kV *Med. Phys.* **41** 042101
- Hernandez A M, Seibert J A, Nosratieh A and Boone J M 2017 Generation and analysis of clinically relevant breast imaging x-ray spectra *Med. Phys.* **44** 2148–60
- James F 2006 *Statistical methods in experimental physics* (Singapore: World Scientific Printers)
- Koning A J and Rochman D 2008 Towards sustainable nuclear energy: putting nuclear physics to work *Ann. Nucl. Energy* **35** 2024–30
- Kurková D and Judas L 2015 X-ray tube spectra measurement and correction using a CdTe detector and an analytic response matrix for photon energies up to 160 keV *Radiat. Meas.* **85** 64–72
- Lépy M C, Duchemin B and Morel J 1994 Comparison of experimental and theoretical L x-ray emission probabilities of <sup>241</sup>Am, <sup>239</sup>Pu and <sup>240</sup>Pu *Nucl. Inst. Methods Phys. Res. A* **353** 10–5
- Lépy M C, Pearce A and Sima O 2015 Uncertainties in gamma-ray spectrometry *Metrologia* **52** S123–45
- Li R, Li L and Chen Z 2017 Spectrum reconstruction method based on the detector response model calibrated by x-ray fluorescence *Phys. Med. Biol.* **62** 1032–45
- Miyajima S and Imagawa K 2002 CdZnTe detector in mammographic x-ray spectroscopy *Phys. Med. Biol.* **47** 3959–72
- Morales M, Bonifácio D A B, Bottaro M and Pereira M A G 2007 Monte Carlo and least-squares methods applied in unfolding of x-ray spectra measured with cadmium telluride detectors *Nucl. Instruments Methods Phys. Res. Sect. A Accel. Spectrometers, Detect. Assoc. Equip.* **580** 270–3
- Ng K P, Kwok C S and Tang F H 2000 Monte Carlo simulation of x-ray spectra in mammography *Phys. Med. Biol.* **45** 1309–18
- Pernicka F and McLean I D 2007 *Dosimetry in diagnostic radiology: an international code of practice* TRS 457 (Vienna: IAEA)
- Poletti M E, Gonçalves O D and Mazzaro I 2002 X-ray scattering from human breast tissues and breast-equivalent materials *Phys. Med. Biol.* **47** 47–63

- Poludniowski G G 2007 Calculation of x-ray spectra emerging from an x-ray tube. Part II. x-ray production and filtration in x-ray targets *Med. Phys.* **34** 2175–86
- Poludniowski G G and Evans P M 2007 Calculation of x-ray spectra emerging from an x-ray tube. Part I. Electron penetration characteristics in x-ray targets *Med. Phys.* **34** 2164–74
- Poludniowski G, Landry G, DeBlois F, Evans P M and Verhaegen F 2009 SpekCalc: a program to calculate photon spectra from tungsten anode x-ray tubes *Phys. Med. Biol.* **54** N433–8
- Salehi Z, Ya Ali N K and Yusoff A L 2012 X-ray spectra and quality parameters from Monte Carlo simulation and analytical filters *Appl. Radiat. Isot.* **70** 2586–9
- Salvat F, Fernández-Varea J and Sempau J 2011 *PENELOPE-2011: A code system for Monte Carlo simulation of electron and photon transport* (Barcelona: Universitat de Barcelona)
- Salvat F, Sempau J, Fernández-Varea J M and Josep S 2015 *PENELOPE-2014: A code system for Monte Carlo simulation of electron and photon transport* (Barcelona: Universitat de Barcelona)
- Santos J C, Mariano L, Tomal A and Costa P R 2016 Evaluation of conversion coefficients relating air-kerma to  $H^*(10)$  using primary and transmitted x-ray spectra in the diagnostic radiology energy range *J. Radiol. Prot.* **36** 117–32
- Santos J C, Tomal A, Furquim T A, Fausto A M F, Nogueira M S and Costa P R 2017 Direct measurement of clinical mammographic x-ray spectra using a CdTe spectrometer *Med. Phys.* **44** 3504–11
- Sempau J, Badal A and Brualla L 2011 A PENELOPE based system for the automated Monte Carlo simulation of clinacs and voxelized geometries, application to far from axis fields *Med. Phys.* **38** 5887
- Steinbauer E, Bauer P and Biersack J 1990 Monte Carlo simulations of RBS spectra: comparison to experimental and empirical results *Nucl. Instruments Methods Phys. Res. B* **45** 171–5
- Taleei R and Shahriari M 2009 Monte Carlo simulation of x-ray spectra and evaluation of filter effect using MCNP4C and FLUKA code *Appl. Radiat. Isot.* **67** 266–71
- Tomal A, Cunha D M, Antoniassi M and Poletti M E 2012 Response functions of Si(Li), SDD and CdTe detectors for mammographic x-ray spectroscopy *Appl. Radiat. Isot.* **70** 1355–9
- Tomal A, Santos J C, Costa P R, Lopez Gonzales A H and Poletti M E 2015 Monte Carlo simulation of the response functions of CdTe detectors to be applied in x-ray spectroscopy *Appl. Radiat. Isot.* **100** 32–7
- Vidal M, Ibáñez P, Guerra P, Valdivieso-Casique M F, Rodriguez R, Illana C and Udias J M 2019 Fast optimized Monte Carlo phase-space generation and dose prediction for low energy x-ray intra-operative radiation therapy *Phys. Med. Biol.* **64** 075002
- Waghorn B J, Meeks S L and Langen K M 2011 Analyzing the impact of intrafraction motion: correlation of different dose metrics with changes in target D95 *Med. Phys.* **38** 4505–11
- White D R, Martin R J and Darlison R 1977 Epoxy resin based tissue substitutes *Br. J. Radiol.* **50** 814–21